frontiers in Materials

ORIGINAL RESEARCH
published: 09 March 2022
doi: 10.3389/fmats.2022.875684

Nitrogen, Phosphorus, and Sulfur Tri-doped Carbon A Coated $NiCo_2Se_4$ Needle Arrays Grown on Carbon Cloth as Binder-free Anode for Potassium-Ion Batteries

*Jinchen Fan[1,2], Yujun Zheng[2], Zhongshu Zhao[2], Wenyao Guo[2] and Sheng Zhu[2]**

[1]School of Materials and Chemistry, University of Shanghai for Science and Technology, Shanghai, China, [2]Shanghai Key Laboratory of Materials Protection and Advanced Materials in Electric Power, College of Environmental and Chemical Engineering, Shanghai University of Electric Power, Shanghai, China

Bimetallic selenides are considered to be the promising high-capacity anode materials for potassium ion batteries (PIBs). However, the dramatic volume fluctuation of K^+ ions and pulverization during cycling still limit their practical application in PIBs. Herein, the nitrogen, phosphorus, and sulfur tri-doped carbon (SPNC)-coated bimetallic $NiCo_2Se_4$ needle arrays grown on carbon cloth ($NiCo_2Se_4$⊂SPNC/CC) prepared as a binder-free anode for PIBs. The polyphosphazene (PSZ) was used as ingenious heteroatoms doping carbon source. The coated SPNC layer derived from the PSZ on the surfaces of $NiCo_2Se_4$ needle arrays not only effectively alleviate the volume expansion of $NiCo_2Se_4$ but also provide abundant active sites for the storage of K^+ ions. As the PIB anode, the $NiCo_2Se_4$⊂SPNC/CC could deliver a high reversible capacity of 880.9 mA h g^{-1} at a current density of 0.1 A g^{-1}. After 500 cycles, the $NiCo_2Se_4$⊂SPNC/CC anode still maintains a high reversible capacity of 268.1 mA h·g^{-1} at a current density of 0.5 A g^{-1}.

Keywords: potassium-ion batteries, bimetallic selenides, tri-doped carbon, carbon cloth, binder-free anode

OPEN ACCESS

Edited by:
Likun Pan,
East China Normal University, China

Reviewed by:
Shuangqiang Chen,
Shanghai University, China
Hongbo Shu,
Xiangtan University, China

****Correspondence:***
Sheng Zhu
zhusheng@shiep.edu.cn

Specialty section:
This article was submitted to Energy Materials, a section of the journal Frontiers in Materials

Received: *14 February 2022*
Accepted: *23 February 2022*
Published: *09 March 2022*

Citation:
Fan J, Zheng Y, Zhao Z, Guo W and Zhu S (2022) Nitrogen, Phosphorus, and Sulfur Tri-doped Carbon A Coated $NiCo_2Se_4$ Needle Arrays Grown on Carbon Cloth as Binder-free Anode for Potassium-Ion Batteries. Front. Mater. 9:875684. doi: 10.3389/fmats.2022.875684

INTRODUCTION

With the rapid development of portable electronic equipment and electric vehicles, the demand for energy storage devices with high energy density and high safety is increasing. Among the large-scale energy storage devices, lithium-ion batteries (LIBs) have attracted extensive attention due to their high energy density, environmental friendliness, and high efficiency. Due to insufficient lithium resources, researchers turned their attention to resource-rich potassium-ion batteries (PIBs) (Hu et al., 2017; Ge et al., 2018). Compared to the LIBs, PIBs have similar energy storage mechanisms, moreover, have the advantages of low production cost and low reduction potential (relative to the standard hydrogen electrode ≈2.94 V) (Liu et al., 2020; Rajagopalan et al., 2020). Therefore, PIBs are expected to become an alternative to LIBs(Zhao et al., 2021). Obtaining the high energy density of PIBs mainly depends on technological breakthroughs in electrode materials. However, toward the PIBs, due to the large radius of potassium ions, the kinetics of K^+ during the intercalation/delamination process is slow and the volume is prone to expansion, which will cause the battery's capacity to decay rapidly and the decrease of coulomb efficiency (Zhang et al., 2021). The key to improving the performance of PIBs is to develop an anode material with excellent electrochemical performance (Zheng et al., 2021).

Among the various explored anode materials, transition metal compounds show great potential due to their excellent electrochemical performance. Compared to the transition metal sulfides and oxides, transition metal selenides have a narrower band gap and a higher volumetric capacity (Qiu et al., 2020). Moreover, the metal-Se bond in the metal selenide is weak and easy to break, which is beneficial to the conversion reaction (Zhu et al., 2017; Hou et al., 2018; Xie et al., 2019; Luo et al., 2020). $NiCo_2Se_4$ as a kind of bimetallic selenides is widely used as PIB anodes because of its rich electronic reaction processes, high conductivity, and excellent chemical stability. Nevertheless, $NiCo_2Se_4$ still has some problems, such as pulverization of the electrode material due to volume expansion during charging and discharging, which causes the battery's capacity to rapidly decay. In view of these problems, how to solve the volume change during the continuous intercalation and delamination of K^+ ions are the main challenge to improve the electrochemical performance and cycle stability of PIBs. In order to solve the above-mentioned problems of $NiCo_2Se_4$, Zhou *et al.* deposited the hierarchical $NiCo_2Se_4$ nanoneedles/nanosheets on the skeleton of N-doped three-dimensional porous graphene (NPG) as sodium-ion battery anode and found that the high conductivity and porous NPG improves the transport of electrons of the anode as well as ions (Zhou et al., 2021). Always, incorporating the carbonaceous materials is considered to be the competitive way to improve the cycling performance and rate capability of PIB anode materials. Huang *et al.* designed the hierarchical carbon-coated $MoSe_2$/MXene hybrid nanosheets ($MoSe_2$/MXene@C) as anode material for PIBs(Huang et al., 2019). The coated carbon layer reinforced the composite structure of $MoSe_2$/MXene, meantime enhancing the overall conductivity of the hybrid $MoSe_2$/MXene@C, which finally promoted the charge-transfer kinetics and improved the durability of PIB.

Herein, the nitrogen, phosphorus, and sulfur tri-doped carbon-coated $NiCo_2Se_4$ needle arrays grown on carbon cloth ($NiCo_2Se_4$⊂SPNC/CC) was prepared as a binder-free anode for PIBs. The $NiCo_2Se_4$⊂SPNC/CC owns an internally hierarchical stable structure, which is composed of CC as the base, $NiCo_2Se_4$ needle arrays as the middle active layer, and an outer layer of nitrogen, phosphorus, and sulfur tri-doped carbon layers (SPNC) which effectively alleviate the powdering and volume expansion of the anode material of $NiCo_2Se_4$ during the charging and discharging process. The coating of SPNC could improve the conductivity of the anode and the doping of S, P, and N provide abundant active sites for the storage of potassium ions. The $NiCo_2Se_4$⊂SPNC/CC anode exhibits high reversible capacity, excellent cycle stability, and good rate performance.

EXPERIMENTAL

Chemicals and Materials

Cobalt nitrate hexahydrate ($Co.(NO_3)_2{\cdot}6H_2O$, 99.0%) and nickel nitrate hexahydrate ($Ni(NO_3)_2{\cdot}6H_2O$, 99.0%) and Urea (CH_4N_2O, 99.0%) were provided from Shanghai Titan Technology Co., Ltd. Hexachlorocyclotriphosphazene (HCCP, 99%), 4, 4′-dihydroxydiphenylsulfone (BPS, 99%) and triethylamine (TEA, 99.7%) were purchased from Shanghai Aladdin Biochemical Technology Co., Ltd. The carbon cloth (Ce-tech, W0S1002) was purchased from Phychemi Company Limited.

Instruments and Characterization

The morphologies for the CC, $NiCo_2O_4$/CC, and $NiCo_2Se_4$⊂SPNC/CC were characterized by a field emission scanning electron microscope (SEM) (JEOL JEM-7800F). The X-ray diffraction (XRD) patterns of the CC, $NiCo_2O_4$/CC, and $NiCo_2Se_4$⊂SPNC/CC were recorded on a Bruker AXS D8 Advance diffractometer. The XPS spectrum of the $NiCo_2Se_4$⊂SPNC/CC was performed from the Thermo Scientific ESCALAB 250Xi using Al Kα radiation.

Synthesis of the $NiCo_2O_4$/CC

Firstly, the carbon cloth (CC) was pretreated in mixture acid of concentrated nitric acid (HNO_3) and concentrated sulfuric acid (H_2SO_4) (3:1, *v/v*) at 80°C for 6 h. After that, the CC was rinsed with plenty of water. The $NiCo_2O_4$/CC was prepared by a one-step hydrothermal reaction. 0.291 g of $Co.(NO_3)_2{\cdot}6H_2O$, 0.145 g of $Ni(NO_3)_2{\cdot}6H_2O$, and 0.27 g of urea were weighed and then added into 30 ml of deionized water under magnetic stirring. After stirring for 30 min, the obtained pink precursor mix solution was transferred into a 50 ml Teflon-lined stainless-steel autoclave. Successively, the pretreated CC was immersed into the aforementioned solution and reacted at 120°C for 6 h. After being naturally cooled to room temperature, the $NiCo_2O_4$/CC was taken out and washed with deionized water and ethanol several times. Finally, the $NiCo_2O_4$/CC was vacuum dried at 60°C for 12 h.

Preparation of the $NiCo_2O_4$⊂SPNC/CC

The $NiCo_2O_4$⊂SPNC/CC was prepared from the carbonization of polyphosphazenes-coated $NiCo_2O_4$/CC. The polyphosphazenes (PSZ)-coated $NiCo_2O_4$/CC ($NiCo_2O_4$⊂PSZ/CC) were synthesized via *in situ* polymerization. The dried $NiCo_2O_4$/CC was first soaked in 30 ml of anhydrous acetonitrile. Then, 0.025 g of hexachlorocyclotriphosphazene (HCCP) and 55.7 mg of 4, 4′-dihydroxydiphenylsulfone (BPS) were added with stirring. Subsequently, 10 μL of triethylamine was added to the solution. After a polycondensation of 6 h, the $NiCo_2O_4$⊂PSZ/CC was then vacuum dried at 60°C for 12 h. Then, the dried $NiCo_2O_4$⊂PSZ/CC was carbonized at 600 °C for 2 h under N_2 atmosphere with a heating rate of $2°C{\cdot}min^{-1}$. After the carbonization, the $NiCo_2O_4$⊂SPNC/CC was successfully obtained.

Fabrication of the $NiCo_2Se_4$⊂SPNC/CC

The $NiCo_2Se_4$⊂SPNC/CC were hydrothermally selenizated from the $NiCo_2O_4$⊂SPNC/CC. A 120 mg of selenium (Se) powder was slowly added into 5 ml of hydrazine hydrate ($N_2H_4{\cdot}H_2O$) under magnetic stirring. Then, the Se solution was slowly dropwise added into 20 ml of deionized water under magnetic stirring. In the next, the $NiCo_2O_4$⊂SPNC/CC were immersed into the above solution and transferred into a 50 ml Teflon-lined stainless-steel

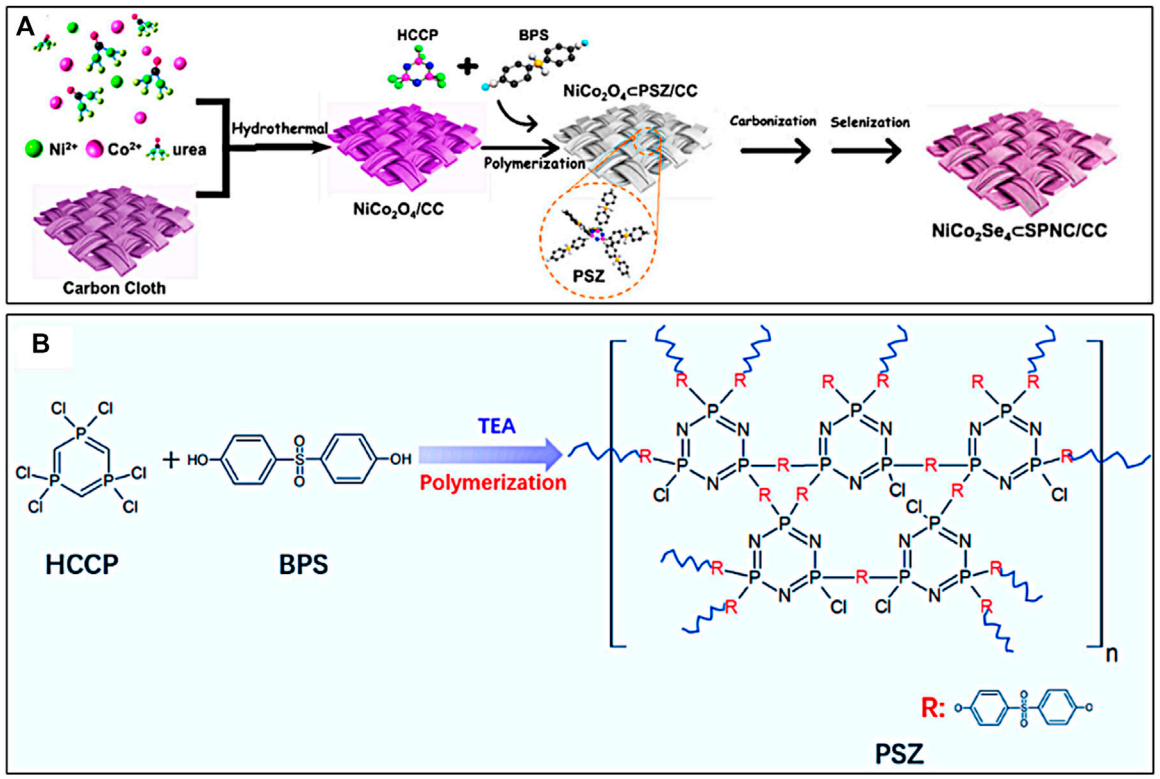

FIGURE 1 | (A) Schematic illustration for the preparation of $NiCo_2Se_4$⊂SPNC/CC and **(B)** the poly-condensation process of HCCP and BPS in the presence of TEA.

autoclave and reacted at 200°C for 10 h. After cooling to room temperature, the $NiCo_2Se_4$⊂SPNC/CC was carefully washed several times with ethanol and deionized water and dried under vacuum at 60°C for 12 h.

Electrochemical Test

Electrochemical measurements were carried out in CR2032 type coin cells at room temperature. The working electrodes were prepared by mixing 80 wt% of active materials, 10 wt% of Super-P carbon black, and 10 wt% of poly (vinylidene fluoride) (PVDF). Cu foil was employed as the current collector, and the electrodes were directly punched into a disc with a diameter of 14 mm. The active substance loading of carbon cloth on the electrode was approximately 2.5 mg cm^{-2}, which was calculated by weighing on a balance. Fresh K foils were used as reference and counter electrodes, and Whatman R glass fibers were used as the separator mats. The electrolyte was a 1.0 M potassium bis(fluorosulfonyl)imide (KFSI) dissolved in a mixture of ethyl carbonate (EC) and dimethyl carbonate (DEC) with a volume ratio of 1:1. The coin cells were assembled in an Ar-filled glovebox (universal 2,440, MIKROUNA), in which both moisture and oxygen levels were below 1 ppm. CV at a scan rate from 0.1 to 1.2 mV s^{-1} and EIS in the frequency range from 0.01 to 10^5 Hz were carried out using an electrochemical workstation (CHI 660D, CHI Instrument). Galvanostatic discharge-charge tests were performed between 0.01 and 3.0 V on a battery testing system (CT 2001A, Land).

RESULTS AND DISCUSSION

As shown in **Figure 1A**, the preparation process of $NiCo_2Se_4$⊂SPNC/CC was mainly divided into three steps. In the first step, the $NiCo_2O_4$/CC was synthesized via hydrothermal reaction. From **Figure 2A,B**, the surfaces of the carbon fibers of CC are clean and smooth. After the hydrothermal reaction, it is obvious that the $NiCo_2O_4$ nanoneedle arrays with the mean root width of ~85 nm and length of ~1.5 μm are grown on the carbon fibers of CC (**Figure 2C**). Secondly, the surfaces of $NiCo_2O_4$/CC have coated the polymer layers of the polyphosphazene (PSZ) *via in-situ* polycondensation of hexachlorotripolyphosphazene (HCCP) and 4,4′-dihydroxydiphenylsulfone (BPS) (**Figure 1B**), which is demonstrated by the Fourier transform infrared spectroscopy (FTIR) spectra (**Supplementary Figure S1**). After the following carbonization in an N_2 atmosphere at 600 °C for 2 h, the obtained $NiCo_2O_4$⊂SPNC/CC were further converted into $NiCo_2Se_4$⊂PSZ/CC by using solvothermal selenization at 200°C for 10 h. From **Figure 2E,F**, after selenization and carbonization, the $NiCo_2Se_4$ needles were connected by the layers of SPNC and the surfaces of $NiCo_2O_4$ nanoneedle arrays become very rough.

Figure 3 shows the XRD patterns for the CC, $NiCo_2O_4$/CC, and $NiCo_2Se_4$⊂SPNC/CC. For the XRD patterns of the pure CC and $NiCo_2O_4$/CC, there are evident diffraction peaks at $2\theta = 26.2^o$ which are ascribed to the C (002) plane of graphite carbon. For the XRD pattern of $NiCo_2Se_4$⊂SPNC/CC, the diffraction peaks at

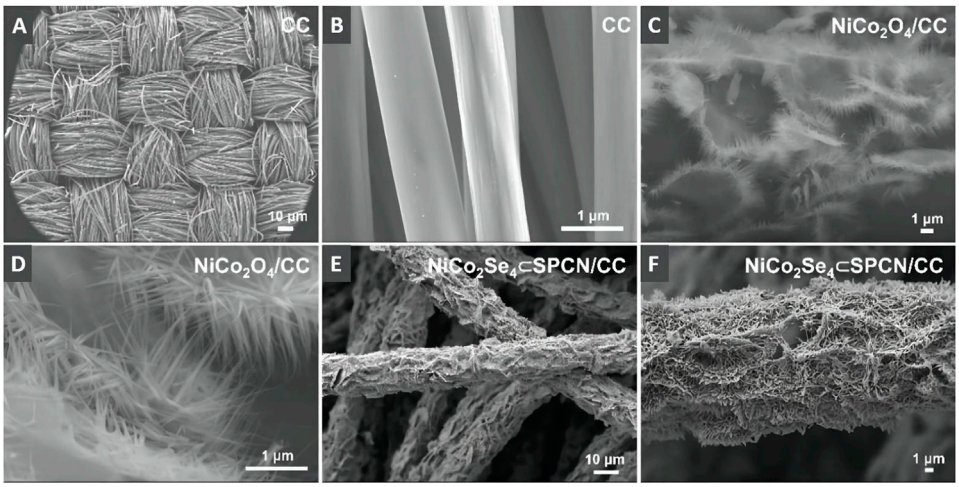

FIGURE 2 | SEM images for the **(A,B)** pure CC **(C,D)** $NiCo_2O_4$/CC, and **(E,F)** $NiCo_2Se_4$⊂SPNC/CC.

2θ = 33.7°, 45.3°, and 51.2° are attributed to the (101), (102) and (110) crystal planes of the monoclinic $NiCo_2Se_4$ phase standard card (JCPDS No. 08–4821), demonstrating the formation of $NiCo_2Se_4$(Zhang et al., 2020). It is worth noting that the diffraction peaks of the C (002) plane of $NiCo_2Se_4$⊂SPNC/CC moves to the relatively lower diffraction angles which are attributed to the increase of interplanar spacing after the introduction of nitrogen, phosphorus, and sulfur heteroatoms (Li et al., 2019). X-ray photoelectron spectroscopy (XPS) spectrum for the $NiCo_2Se_4$⊂SPNC/CC was further used to characterize the valence states and surface chemical composition. From the XPS survey spectrum, the Ni, Co., Se, N, S, P, C, and O elements exist in the $NiCo_2Se_4$⊂SPNC/CC (**Figure 3B**). In the Co. 2p spectrum (**Figure 3C,D**), there are six cobalt chemical states. The peaks at binding energies of 785.6 and 802.1 eV correspond to the satellite peaks (Yu et al., 2019). The spin-orbit peaks of Co^{2+} and Co^{3+} are located at 778.9, 793.8 eV, and 781.4, 797.1 eV, respectively (Guan et al., 2019). Similarly, toward the Ni 2p spectrum, there are also two satellite peaks which are appeared at 861.7 and 882.2 eV (Zeng et al., 2017). The two pair's peaks at 853.8, 872.7 eV and 856.3, 877.5 eV are ascribed to the spin-orbit peaks of Ni^{2+} and Ni^{3+}(Xu et al., 2020). In **Figure 3E**, the peaks at 55.6 and 54.7 eV correspond to the spin-orbit peaks of Se $3d_{3/2}$ and Se $3d_{5/2}$. A broad peak at 59.4 eV can be related to the SeO_x (Chong et al., 2021). The C 1s high-resolution XPS spectrum is depicted in **Figure 3F**, which can be fitted into four peaks including C-C/C=C (284.4 eV), C–N or C–S (285.9 eV), C-P (287.1 eV), and O=C-O (290.1 eV). As illustrated in **Figure 3G**, the peak at 161.2 eV is assigned to the C-S-C bonding in the PSZ-derived carbon framework (Shen et al., 2017). The peak at 166.7 eV is mainly attributed to the oxidation state of sulfur (C–SO_x). By fitting, the P 2p spectrum could split into the P-C and P-O peaks which are located at 133.5 and 137.7 eV (Qian et al., 2019). Besides the S and P elements, the N dopant in the PSZ-derived carbon framework was also confirmed by the N 1s of the XPS spectrum, as shown in **Figure 3I**, the peaks for the pyridinic N, pyrrolic N, and graphitic N are clearly observed at 398.6 400.4 and 402.1 eV (Xu et al., 2021). In addition, the peak of the oxidation state N is located at 403.23 eV (Cui et al., 2020). Based on the above analysis, the N, S, and P elements were successfully doped in the carbon framework, which could be acted as active sites for the storage of potassium ions. The atom percentages of N, S, and P elements are 2.66, 4.23, and 2.3%, respectively.

The K-ion storage behavior of the $NiCo_2Se_4$⊂SPNC/CC anode was first studied by cyclic voltammetry (CV). The CV curves for the first three circles are shown in **Figure 4A** at the scan rate of 0.1 mV·s-1 within the voltage window of 0.01–3 V. In the first cycle, the reduction peak around 0.31 V should be related to the formation of the solid electrolyte interface (SEI) film, and the large reduction band at 1.2 V should be related to the K^+ ion insertion in the structure of $NiCo_2Se_4$ and the formation of $NiCo_2Se_4$($NiCo_2Se_4+xK^++xe^- = K_xNiCo_2Se_4$) (Li et al., 2020). During the first cycle process, the oxidation peaks at 0.54, 1.73, 1.94 and 2.19 V are attributed to the reaction from $K_xNiCo_2Se_4$ to Co., Ni, and K_2Se(Chen et al., 2021). The peak around 0.01–0.03 V in the cathodic scan may be due to the intercalation of K^+ ions in the SPNC layer of the $NiCo_2Se_4$⊂SPNC/CC. In the subsequent cycles, the large reduction band was shifted to 1.44 V which is related to the potassiumization process. The difference between the first and second cycles indicates that the reaction paths of the two cycles are inconsistent, which is the reason for the irreversible capacity in the first cycle. The CV curves almost overlap after the second cycle, indicating the excellent cycle performance of the $NiCo_2Se_4$⊂SPNC/CC electrode.

Figure 4B shows the galvanostatic charge-discharge (GCD) curves for the $NiCo_2Se_4$⊂SPNC/CC electrode in the first, second, third, fifth, and 10th circles at a current density of 0.1 A g^{-1} and applied voltage window of 0.01–3 V. During the initial cycle, a high discharge specific capacity of 1549.2 mA h·g^{-1} was obtained. The first charge specific capacity is 1076.9 mA h·g^{-1}, and the initial Coulombic efficiency is about 69.5%, which is related to the formation of the SEI film on the electrode surface. In addition, the

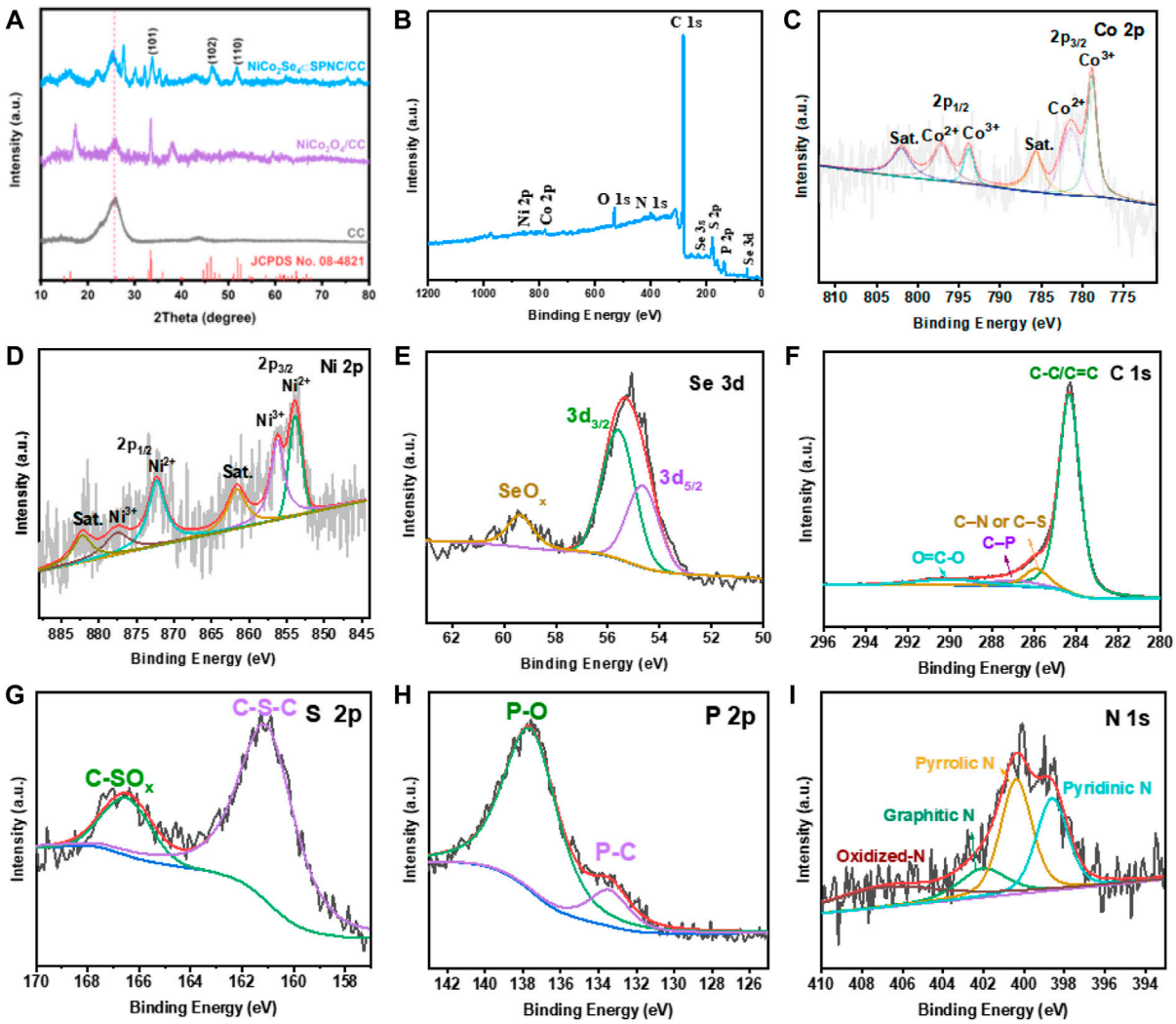

FIGURE 3 | (A) XRD patterns for the CC, $NiCo_2O_4$/CC and $NiCo_2Se_4$⊂SPNC/CC, **(B)** XPS survey spectrum of the $NiCo_2Se_4$⊂SPNC/CC, the high-resolution XPS spectra for **(C)** Co. 2p, **(D)** Ni 2p, **(E)** Se 3days, **(F)** C 1s, **(g)** S 2p, **(H)** P 2p, and **(I)** N 1s.

discharge plateaus of 1.0–1.2 V and 0.2–0.4 V in the first circle are mainly attributed to the formation of $K_xNiCo_2Se_4$ and the conversion reaction from $K_xNiCo_2Se_4$ to Co., Ni, and K_2Se, which is consistent with the CV analysis. The $NiCo_2Se_4$⊂SPNC/CC electrode shows the reversible capacity of ~890.6 mA h·g^{-1} after the end of 10 cycles with a Coulombic efficiency of nearly 100%. Moreover, from the second to the 10th cycle, the GCD curves basically coincide, which also shows the excellent cycle stability of the $NiCo_2Se_4$⊂SPNC/CC electrode. The rate performances test of CC, $NiCo_2O_4$/CC, and $NiCo_2Se_4$⊂SPNC/CC are shown in **Figure 4C**. When the current densities are 0.1, 0.2, 0.5, 1, and 2 A g^{-1}, the reversible discharge capacities of $NiCo_2Se_4$⊂SPNC/CC are 880.9, 591.4, 356.5, 157.4, and 68.5 mA h·g^{-1}, respectively, indicating that the $NiCo_2Se_4$⊂SPNC/CC has good rate performance. Afterward, as the current density recovers to 0.1 A g^{-1} after 50 cycles, the specific capacity recovers to 689.8 mA h g^{-1}, and after 90 cycles it recovers to 968.6 mA h·g^{-1}, which means that potassium ions at high current density the storage performance has not declined. For pure $NiCo_2O_4$/CC, when the current density is restored, the specific capacity cannot be restored to the capacity under the initial current density. The excellent rate of performance of the $NiCo_2Se_4$⊂SPNC/CC is due to the increase in selenization capacity and the heteroatoms doping of S, P, and N in the carbon layer originated from the polyphosphazene, which increases the active sites for K^+ ions storage. More importantly, the coating of the SPNC layer on the surfaces of $NiCo_2Se_4$ improved the structure stability, largely alleviated the volume expansion of anode in the charge-discharge process, and finally improved the cycle performances of KIB. In addition, from the EIS spectra of the $NiCo_2O_4$/CC and $NiCo_2Se_4$⊂SPNC/CC, the radius of the semicircle in the EIS spectrum of the $NiCo_2Se_4$⊂SPNC/CC is significantly smaller than that of $NiCo_2O_4$/CC, implying the selenization and SPNC

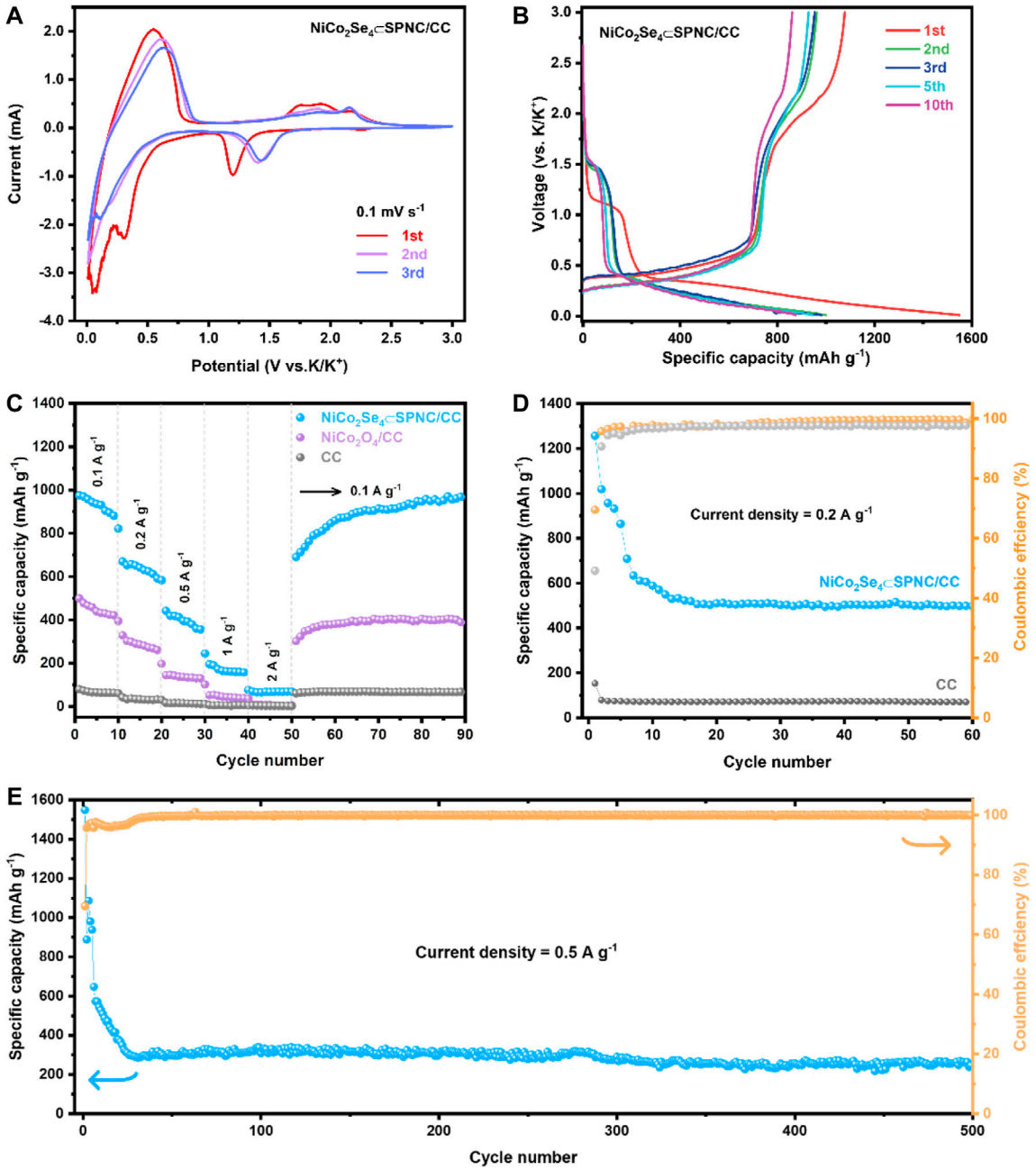

FIGURE 4 | (A) CV curves of the $NiCo_2Se_4$⊂SPNC/CC anode at different scan rates, electrode for the first three circles at 0.1 mV s^{-1}, **(B)** GCD curves for the $NiCo_2Se_4$⊂SPNC/CC electrode in the different circles at a current density of 0.1 A g^{-1}, **(C)** Rate performances of the $NiCo_2Se_4$⊂SPNC/CC electrode, **(D)** Cycle performance and Coulombic efficiency of CC and $NiCo_2Se_4$⊂SPNC/CC at a current density of 0.2 A g^{-1}, and **(E)** Long-term cycling performances of the $NiCo_2Se_4$⊂SPNC/CC anode at a current density of 0.5 A g^{-1}.

coating improved the conductivity and interfacial charge transport (**Supplementary Figure S2**). **Figure 4D** illustrates the cycle performance and Coulombic efficiency of CC and $NiCo_2Se_4$⊂SPNC/CC at the current density of 0.2 A g^{-1}. As a pure carbon material anode, although the CC has a relatively low specific capacity, it has a very good cycling stability electrode. For demonstrating good cycling stability, the cycle performances of CC and $NiCo_2Se_4$⊂SPNC/CC were compared. As shown in **Figure 4E**, the initial specific capacity of the $NiCo_2Se_4$⊂SPNC/CC is ~1256.7 mA h·g^{-1}, and the Coulombic efficiency stabilizes at about 99.7% in the subsequent cycles. After 60 cycles, the specific capacity of the $NiCo_2Se_4$⊂SPNC/CC can still keep at 497.3 mA h·g^{-1}. Further, the long-cycle performance of the $NiCo_2Se_4$⊂SPNC/

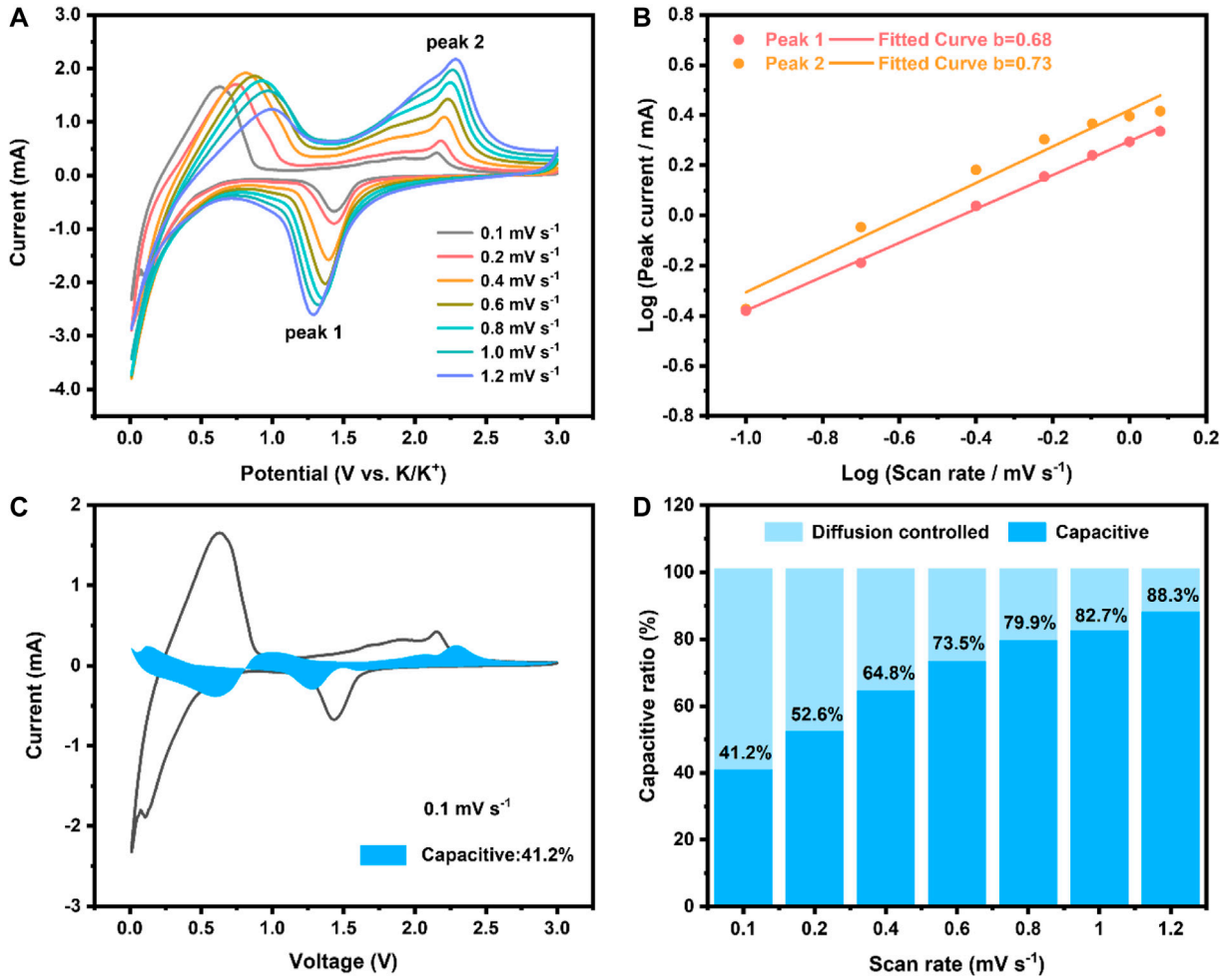

FIGURE 5 | (A) CV curves of the $NiCo_2Se_4$⊂SPNC/CC anode at different scan rates, **(B)** Plots for b-value determination, **(C)** Sketch view of the capacitive behavior of the $NiCo_2Se_4$⊂SPNC/CC anode at 1.0 mV s^{-1}, and **(D)** Contribution rate of pseudocapacitance and diffusion control at different scan rates.

CC was also tested at a current density of 0.5 A g^{-1}. After 500 cycles, the $NiCo_2Se_4$⊂SPNC/CC anode still maintains a high reversible capacity of 268.1 mA h·g^{-1}, and the Coulombic efficiency is close to 100%.

In order to further understand the diffusion dynamics and charge storage of $NiCo_2Se_4$⊂SPNC/CC, the electrochemical kinetics of the $NiCo_2Se_4$⊂SPNC/CC was further studied by CV curves at different scan rates (**Figure 5A**). Increasing with the scan rate, the cathode peak moves to a high potential, and the anode peak moves to a low potential due to the polarization of the electrode at a high current density. The relationship between current and scan rate follows the following formula (Huang et al., 2020):

$$i = av^b \quad (1)$$

$$\log(i) = b\log(v) + \log(a) \quad (2)$$

where a is a constant, and b reflects an adjustable parameter that reflects the mechanism of the charge-storage process. When b = 0.5 or b = 1.0, the charging and discharging process is considered to be controlled by the diffusion control behavior or pseudocapacitance behavior. The value of b calculated from the selected two redox peak potentials is 0.68 and 0.73, respectively (**Figure 5B**), indicating that the electrochemical process of the $NiCo_2Se_4$⊂SPNC/CC anode has the evident diffusion behavior. Toward the structure and morphology of the $NiCo_2Se_4$⊂SPNC/CC anode, the needle-like $NiCo_2Se_4$ array with sufficient void spaces could facilitate the electrolyte penetration and alleviate the effect of the volume change of $NiCo_2Se_4$. And, the coating of the SPNC layer not only formed a conductive network which improves the conductivity and interfacial charge transport, but also provides the heteroatomic active sites for K^+ ions storage. The contribution ratio of pseudocapacitance can be calculated by the following equation (Zhu et al., 2022):

$$i = k_1 v + k_2 v^{1/2} \quad (3)$$

$$i/v^{1/2} = k_1 v^{1/2} + k_2 \quad (4)$$

where k_1v and $k_2v^{1/2}$ refer to the currents of the capacitance and diffusion process, respectively. As shown in **Figure 5C**, the blue shaded part is corresponding to the capacitance current response, and the scan rate is 0.1 mV s^{-1}, where the capacitance contribution is calculated to be ≈41.2%. **Figure 5D** shows the contribution rate of pseudocapacitance and diffusion control at different scan rates. When the scan speed is increased from 0.1 to 1.2 mV s^{-1}, the contribution rate of pseudocapacitance gradually increases from 41.2 to 88.3%, demonstrating that the $NiCo_2Se_4$⊂SPNC/CC anode has a good potassium ion storage capacity during the charge and discharge process.

CONCLUSION

In summary, the $NiCo_2Se_4$⊂SPNC/CC were successfully fabricated by coating the polymer layer of polyphosphazene on the surfaces of $NiCo_2O_4$/CC followed by selenization and carbonization. The polyphosphazene-derived SPNC layer effectively alleviates the volume expansion of $NiCo_2Se_4$ and is beneficial to increase more active sites for the storage of K^+ ions. Based on the effective combination of the SPNC and $NiCo_2Se_4$, the binder-free $NiCo_2Se_4$⊂SPNC/CC anode shows a high reversible capacity of 880.9 mA h·g^{-1} at a current density of 0.1 A g^{-1} as well as good rate performance. Also, the $NiCo_2Se_4$⊂SPNC/CC anode could maintain a high reversible capacity of 268.1 mA h·g^{-1} after 500 cycles, at a current density of 0.5 A g^{-1}. We have reason to believe that the anode materials of multiheteroatoms co-doped bimetallic selenides will show great potential application in PIB batteries.

DATA AVAILABILITY STATEMENT

The raw data supporting the conclusions of this article will be made available by the authors, without undue reservation.

AUTHOR CONTRIBUTIONS

JF: Supervision, Conceptualization, Methodology, Writing original draft. YZ: Writing–review and editing. ZZ: Methodology, Data curation, Investigation. WG: Visualization, Investigation. SZ: Supervision, writing–review and editing.

FUNDING

This research was funded by the National Natural Science Foundation of China (no. 22072088). This work was also sponsored by Shanghai Rising-Star Program (no. 19QA1404100). This work was financially supported by the Science and Technology Commission of Shanghai Municipality (20ZR1421400 and 19DZ2271100).

SUPPLEMENTARY MATERIAL

The Supplementary Material for this article can be found online at: https://www.frontiersin.org/articles/10.3389/fmats.2022.875684/full#supplementary-material.

REFERENCES

Chen, K.-T., Chong, S., Yuan, L., Yang, Y.-C., and Tuan, H.-Y. (2021). Conversion-alloying Dual Mechanism Anode: Nitrogen-Doped Carbon-Coated Bi_2Se_3 Wrapped with Graphene for Superior Potassium-Ion Storage. *Energ. Storage Mater.* 39, 239–249. doi:10.1016/j.ensm.2021.04.019

Chong, X., Liu, C., Wang, C., Yang, R., and Zhang, B. (2021). Integrating Hydrogen Production and Transfer Hydrogenation with Selenite Promoted Electrooxidation of α-Nitrotoluenes to E -Nitroethenes. *Angew. Chem.* 133, 22181–22187. doi:10.1002/ange.202108666

Cui, R. C., Xu, B., Dong, H. J., Yang, C. C., and Jiang, Q. (2020). N/O Dual-Doped Environment-Friendly Hard Carbon as Advanced Anode for Potassium-Ion Batteries. *Adv. Sci.* 7, 1902547. doi:10.1002/advs.201902547

Ge, J., Fan, L., Wang, J., Zhang, Q., Liu, Z., Zhang, E., et al. (2018). MoSe2/N-Doped Carbon as Anodes for Potassium-Ion Batteries. *Adv. Energ. Mater.* 8, 1801477. doi:10.1002/aenm.201801477

Guan, C., Sumboja, A., Zang, W., Qian, Y., Zhang, H., Liu, X., et al. (2019). Decorating Co/CoNx Nanoparticles in Nitrogen-Doped Carbon Nanoarrays for Flexible and Rechargeable Zinc-Air Batteries. *Energ. Storage Mater.* 16, 243–250. doi:10.1016/j.ensm.2018.06.001

Hou, L., Shi, Y., Wu, C., Zhang, Y., Ma, Y., Sun, X., et al. (2018). Monodisperse Metallic $NiCoSe_2$ Hollow Sub-Microspheres: Formation Process, Intrinsic Charge-Storage Mechanism, and Appealing Pseudocapacitance as Highly Conductive Electrode for Electrochemical Supercapacitors. *Adv. Funct. Mater.* 28, 1705921. doi:10.1002/adfm.201705921

Hu, Z., Liu, Q., Chou, S. L., and Dou, S. X. (2017). Advances and Challenges in Metal Sulfides/Selenides for Next-Generation Rechargeable Sodium-Ion Batteries. *Adv. Mater.* 29, 1700606. doi:10.1002/adma.201700606

Huang, H., Cui, J., Liu, G., Bi, R., and Zhang, L. (2019). Carbon-Coated $MoSe_2$/MXene Hybrid Nanosheets for Superior Potassium Storage. *ACS Nano* 13, 3448–3456. doi:10.1021/acsnano.8b09548

Huang, M., Wang, X., Meng, J., Liu, X., Yao, X., Liu, Z., et al. (2020). Ultra-fast and High-Stable Near-Pseudocapacitance Intercalation Cathode for Aqueous Potassium-Ion Storage. *Nano Energy* 77, 105069. doi:10.1016/j.nanoen.2020.105069

Li, K., Chen, S., Chen, S., Liu, X., Pan, W., and Zhang, J. (2019). Nitrogen, Phosphorus Co-doped Carbon Cloth as Self-Standing Electrode for Lithium-Iodine Batteries. *Nano Res.* 12, 549–555. doi:10.1007/s12274-018-2251-1

Li, L., Zhao, J., Zhu, Y., Pan, X., Wang, H., and Xu, J. (2020). Bimetallic Ni/Co-ZIF-67 Derived $NiCo_2Se_4$/N-Doped Porous Carbon Nanocubes with Excellent Sodium Storage Performance. *Electrochim. Acta* 353, 136532. doi:10.1016/j.electacta.2020.136532

Liu, Y., Lu, Y. X., Xu, Y. S., Meng, Q. S., Gao, J. C., Sun, Y. G., et al. (2020). Pitch-Derived Soft Carbon as Stable Anode Material for Potassium Ion Batteries. *Adv. Mater.* 32, 2000505. doi:10.1002/adma.202000505

Luo, M., Yu, H., Hu, F., Liu, T., Cheng, X., Zheng, R., et al. (2020). Metal Selenides for High Performance Sodium Ion Batteries. *Chem. Eng. J.* 380, 122557. doi:10.1016/j.cej.2019.122557

Qian, Y., Jiang, S., Li, Y., Yi, Z., Zhou, J., Li, T., et al. (2019). *In Situ* Revealing the Electroactivity of P-O and P-C Bonds in Hard Carbon for High-Capacity and Long-Life Li/K-Ion Batteries. *Adv. Energ. Mater.* 9, 1901676. doi:10.1002/aenm.201901676

Qiu, L.-C., Wang, Q.-C., Yue, X.-Y., Qiu, Q.-Q., Li, X.-L., Chen, D., et al. (2020). $NiCo_2Se_4$ as an Anode Material for Sodium-Ion Batteries. *Electrochemistry Commun.* 112, 106684. doi:10.1016/j.elecom.2020.106684

Rajagopalan, R., Tang, Y., Ji, X., Jia, C., and Wang, H. (2020). Advancements and Challenges in Potassium Ion Batteries: A Comprehensive Review. *Adv. Funct. Mater.* 30, 1909486. doi:10.1002/adfm.201909486

Shen, H., Gracia-Espino, E., Ma, J., Zang, K., Luo, J., Wang, L., et al. (2017). Synergistic Effects between Atomically Dispersed Fe–N–C and C–S–C for the Oxygen Reduction Reaction in Acidic Media. *Angew. Chem.* 129, 13988–13992. doi:10.1002/ange.201706602

Xie, S., Gou, J., Liu, B., and Liu, C. (2019). Nickel-cobalt Selenide as High-Performance and Long-Life Electrode Material for Supercapacitor. *J. Colloid Interf. Sci.* 540, 306–314. doi:10.1016/j.jcis.2019.01.030

Xu, C., Märker, K., Lee, J., Mahadevegowda, A., Reeves, P. J., Day, S. J., et al. (2020). Bulk Fatigue Induced by Surface Reconstruction in Layered Ni-Rich Cathodes for Li-Ion Batteries. *Nat. Mater.* 20, 84–92. doi:10.1038/s41563-020-0767-8

Xu, Y., Wang, C., Niu, P., Li, Z., Wei, L., Yao, G., et al. (2021). Tuning the Nitrogen-Doping Configuration in Carbon Materials via Sulfur Doping for Ultrastable Potassium Ion Storage. *J. Mater. Chem. A.* 9, 16150–16159. doi:10.1039/d1ta03811g

Yu, P., Wang, L., Sun, F., Xie, Y., Liu, X., Ma, J., et al. (2019). Co Nanoislands Rooted on Co-N-C Nanosheets as Efficient Oxygen Electrocatalyst for Zn-Air Batteries. *Adv. Mater.* 31, 1901666. doi:10.1002/adma.201901666

Zeng, Y., Meng, Y., Lai, Z., Zhang, X., Yu, M., Fang, P., et al. (2017). An Ultrastable and High-Performance Flexible Fiber-Shaped Ni-Zn Battery Based on a Ni-NiO Heterostructured Nanosheet Cathode. *Adv. Mater.* 29, 1702698. doi:10.1002/adma.201702698

Zhang, Y., Li, T., Cao, S.-A., Luo, W., and Xu, F. (2020). $NiCo_2Se_4$ Hierarchical Microflowers of Nanosheets and Nanorods as Pseudocapacitive Mg-Storage Materials. *ACS Sustain. Chem. Eng.* 8, 2964–2972. doi:10.1021/acssuschemeng.9b07592

Zhang, W., Yin, J., Wang, W., Bayhan, Z., and Alshareef, H. N. (2021). Status of Rechargeable Potassium Batteries. *Nano Energy* 83, 105792. doi:10.1016/j.nanoen.2021.105792

Zhao, Z., Gao, C., Fan, J., Shi, P., Xu, Q., and Min, Y. (2021). Dual Confinement of CoSe2 Nanorods with Polyphosphazene-Derived Heteroatom-Doped Carbon and Reduced Graphene Oxide for Potassium-Ion Batteries. *ACS Omega* 6, 17113–17125. doi:10.1021/acsomega.1c02649

Zheng, J., Wu, Y., Sun, Y., Rong, J., Li, H., and Niu, L. (2021). Advanced Anode Materials of Potassium Ion Batteries: From Zero Dimension to Three Dimensions. *Nano-micro Lett.* 13, 1–37. doi:10.1007/s40820-020-00541-y

Zhou, C., Zhang, P., Liu, J., Zhou, J., Wang, W., Li, K., et al. (2021). Hierarchical NiCo2Se4 Nanoneedles/nanosheets with N-Doped 3D Porous Graphene Architecture as Free-Standing Anode for superior Sodium Ion Batteries. *J. Colloid Interf. Sci.* 587, 260–270. doi:10.1016/j.jcis.2020.12.015

Zhu, S., Li, Q., Wei, Q., Sun, R., Liu, X., An, Q., et al. (2017). NiSe2 Nanooctahedra as an Anode Material for High-Rate and Long-Life Sodium-Ion Battery. *ACS Appl. Mater. Inter.* 9, 311–316. doi:10.1021/acsami.6b10143

Zhu, L., Wang, Y., Wang, M., Huang, M., Huang, Y., Zhang, Z., et al. (2022). High Edge-Nitrogen-Doped Porous Carbon Nanosheets with Rapid Pseudocapacitive Mechanism for Boosted Potassium-Ion Storage. *Carbon* 187, 302–309. doi:10.1016/j.carbon.2021.11.021

Conflict of Interest: The authors declare that the research was conducted in the absence of any commercial or financial relationships that could be construed as a potential conflict of interest.

Publisher's Note: All claims expressed in this article are solely those of the authors and do not necessarily represent those of their affiliated organizations, or those of the publisher, the editors and the reviewers. Any product that may be evaluated in this article, or claim that may be made by its manufacturer, is not guaranteed or endorsed by the publisher.